Journal of Geophysical Research: Space Physics

RESEARCH ARTICLE
10.1029/2018JA025226

Global Model of Plasmaspheric Hiss From Multiple Satellite Observations

Nigel P. Meredith[1], **Richard B. Horne**[1], **Tobias Kersten**[1], **Wen Li**[2], **Jacob Bortnik**[3], **Angélica Sicard**[4], **and Keith H. Yearby**[5]

[1]British Antarctic Survey, Natural Environment Research Council, Cambridge, England, [2]Center for Space Physics, Boston University, Boston, MA, USA, [3]Department of Atmospheric and Oceanic Sciences, University of California, Los Angeles, CA, USA, [4]Office National d'Etudes et Recherches Aérospatiales, Toulouse, France, [5]Department of ACSE, University of Sheffield, UK

Abstract We present a global model of plasmaspheric hiss, using data from eight satellites, extending the coverage and improving the statistics of existing models. We use geomagnetic activity dependent templates to separate plasmaspheric hiss from chorus. In the region 22–14 magnetic local time (MLT) the boundary between plasmaspheric hiss and chorus moves to lower L^* values with increasing geomagnetic activity. The average wave intensity of plasmaspheric hiss is largest on the dayside and increases with increasing geomagnetic activity from midnight through dawn to dusk. Plasmaspheric hiss is most intense and spatially extended in the 200 to 500 Hz frequency band during active conditions, $400 < AE < 750$ nT, with an average intensity of 1,128 pT^2 in the region 05–17 MLT from $1.5 < L^* < 3.5$. In the prenoon sector, waves in the 100 to 200 Hz frequency band peak near the magnetic equator and decrease in intensity with increasing magnetic latitude, inconsistent with a source from chorus outside the plasmapause, but more consistent with local amplification by substorm-injected electrons. At higher frequencies the average wave intensities in this sector exhibit two peaks, one near the magnetic equator and one at high latitudes, $45° < |\lambda_m| < 60°$, with a minimum at intermediate latitudes, $30° < |\lambda_m| < 40°$, consistent with a source from chorus outside the plasmapause. In the premidnight sector, the intensity of plasmaspheric hiss in the frequency range $50 < f < 1{,}000$ Hz decreases with increasing geomagnetic activity. The source of this weak premidnight plasmaspheric hiss is likely to be chorus at larger L^* in the postnoon sector that enters that plasmasphere in the postnoon sector and subsequently propagates eastward in MLT.

Key Points:
- Hiss is most intense and spatially extended in the 200 to 500 Hz frequency band during active conditions
- In the prenoon sector hiss above 200 Hz peaks near the equator and at high latitude consistent with a source from chorus at higher L^*
- The source of weak premidnight hiss is likely to be chorus at larger L^* in the postnoon sector

Correspondence to:
N. P. Meredith,
nmer@bas.ac.uk

Citation:
Meredith, N. P., Horne, R. B., Kersten, T., Li, W., Bortnik, J., Sicard, A., & Yearby, K. H. (2018). Global model of plasmaspheric hiss from multiple satellite observations. *Journal of Geophysical Research: Space Physics*, *123*, 4526–4541. https://doi.org/10.1029/2018JA025226

Received 12 JAN 2018
Accepted 1 MAY 2018
Accepted article online 10 MAY 2018
Published online 5 JUN 2018

1. Introduction

Plasmaspheric hiss is a broadband electromagnetic emission typically observed in the frequency range from ~10 Hz to several kilohertz (Li et al., 2015). This emission is characteristically restricted to high density regions, namely, the plasmasphere (Dunckel & Helliwell, 1969; Russell et al., 1969; Thorne et al., 1973) and plasmaspheric plumes (Chan & Holzer, 1976; Cornilleau-Wehrlin et al., 1978; Parrot & Lefeuvre, 1986; Summers et al., 2008). Plasmaspheric hiss persists during geomagnetically quiet times (Carpenter, 1978; Thorne et al., 1977) but intensifies during geomagnetic storms (Smith et al., 1974; Tsurutani et al., 1975) and substorms (Meredith et al., 2004; Thorne et al., 1973).

Broadband amplitudes of plasmaspheric hiss typically range from 10 pT or less during quiet conditions to >100 pT during active periods (Meredith et al., 2004; Smith et al., 1974; Thorne et al., 1974, 1977). Plasmaspheric hiss is observed at all local times but tends to maximize on the dayside during geomagnetically active conditions (Li et al., 2015; Meredith, Horne, Glauert, et al., 2006; Meredith et al., 2004; Tsurutani et al., 2015). Plasmaspheric hiss is found to propagate over a wide range of wave normal angles, with predominantly field aligned propagation near the magnetic equator and more oblique propagation at higher latitudes (Agapitov et al., 2013; Parrot & Lefeuvre, 1986; Santolík et al., 2001). The emissions have traditionally been thought of as incoherent although cases of coherent waves have recently been reported (Summers et al., 2014; Tsurutani et al., 2015).

Plasmaspheric hiss is an important magnetospheric emission due to its role in radiation belt dynamics. It is largely responsible for the formation of the slot region between the inner and the outer radiation belt

(Albert, 1994; Abel & Thorne, 1998a, 1998b; Lyons & Thorne, 1973; Lyons et al., 1972; Meredith et al., 2007, 2009). Further out, scattering by plasmaspheric hiss contributes to electron loss during geomagnetic storms (Lam et al., 2007; Summers et al., 2007) and can explain the quiet time decay of outer radiation belt electrons (Lam et al., 2007; Meredith, Horne, Glauert, et al., 2006). More recently, Thorne et al. (2013) showed that plasmaspheric hiss could explain the slow decay of the unusual narrow ring of multi-MeV electrons following the September 2012 geomagnetic storm.

The origin of plasmaspheric hiss has been a subject of active debate for over 40 years (e.g., Bortnik, Thorne, et al., 2009). Recent studies suggest that plasmaspheric hiss is generated by a number of different mechanisms that largely depend on frequency. Plasmaspheric hiss below 150 Hz, which is observed close to the plasmapause and reaches peak amplitudes near 15 magnetic local time (MLT) (Malaspina et al., 2017), is thought to be generated by local amplification of the background whistler mode noise due to substorm-injected electrons in the outer plasmasphere (Chen et al., 2014; Li et al., 2013). At higher frequencies, plasmaspheric hiss in the frequency range 150 Hz $< f <$ 2,000 Hz is found to extend further Earthward and reaches peak amplitudes near 12 MLT (Malaspina et al., 2017). Plasmaspheric hiss in this frequency range is thought to originate from bursts of short duration (~0.1 s) chorus emissions that are excited outside the plasmapause and then propagate into and become trapped inside the plasmasphere (Bortnik et al., 2008; Bortnik, Li, et al., 2009; Chen et al., 2012a, 2012b). At higher frequencies ($2 < f < 5$ kHz) the waves inside the plasmapause are more correlated with land mass, where most lightning occurs, and are likely generated by lightning in thunderstorms as lightning generated whistlers (Meredith, Horne, Clilverd, et al., 2006). However, there is also a population of waves observed in this frequency range that peaks on the dayside during active conditions (Meredith et al., 2007) and is most likely generated by chorus outside of the plamapause.

Plasmaspheric hiss can be organized by a combination of distance from the plasmapause and plasmapause distance from Earth (Malaspina et al., 2016), but radiation belt models generally use a coordinate system based on the adiabatic invariants and require wave intensities as a function of position and geomagnetic activity. In order to use a model of plasmaspheric hiss based on distance from the plasmapause and distance of the plasmapause from Earth models of the wave intensity in this coordinate system as a function of magnetic local time and magnetic latitude would be required together with an accurate model of plasmapause position as a function of MLT and geomagnetic activity. Further developments of this potential method are thus required before a technique based on the distance from the plasmapause and plasmapause distance from Earth can be tested against existing models based on magnetic coordinates and geomagnetic activity. In this study we model the average intensity of plasmaspheric hiss as a function of spatial location in magnetic coordinates and geomagnetic activity as monitored by the *AE* index.

Previous models of plasmaspheric hiss based on the analysis of the Combined Release and Radiation Effects Satellite (CRRES) plasma wave observations (Glauert et al., 2014a, 2014b; Meredith et al., 2004) have some limitations due to limited frequency coverage, limited spatial coverage on the dayside, and perhaps most significantly, lack of wave magnetic field measurements. In these former studies the wave magnetic field was derived from the measured wave electric field using the cold plasma dispersion relation assuming parallel propagation. The effects of plasmaspheric hiss propagating at different wave normal angles on electron loss rates were examined in Meredith, Horne, Glauert, et al. (2006) and Meredith et al. (2007) where it was shown that the observed loss rates could be explained by waves propagating at small and intermediate wave normal angles but that highly oblique waves overestimated the loss time scales by over an order of magnitude. Recent theoretical and modeling studies have shown that parallel propagation is a reasonable approximation for waves near the magnetic equator but not at intermediate magnetic latitudes ($15° < |\lambda_m| < 30°$) where the wave normal angle can become highly oblique (Agapitov et al., 2013; Glauert et al., 2014a; Ni et al., 2013). For this study we exclude the CRRES plasma wave data from the analysis so that we do not require a conversion from wave electric to magnetic field through a potentially inaccurate assumption. The results can then be compared with the results from a model of plasmaspheric hiss based on CRRES measurements alone to see where the agreement is good and where it is likely to break down.

There are several dynamic global radiation belt models that are based on diffusion models (Albert et al., 2009; Fok et al., 2008; Glauert et al., 2014a; Li et al., 2016; Ma et al., 2015; Su et al., 2011; Subbotin et al., 2010; Tu et al., 2014; Varotsou et al., 2005, 2008). These models all require diffusion rates for the relevant wave modes, including whistler mode chorus, magnetosonic waves, plasmaspheric hiss, lightning generated whistlers, and electromagnetic ion cyclotron waves (e.g., Thorne, 2010). Diffusion rates are proportional to the wave magnetic field intensity, which in turn, for any given wave mode, can vary significantly with both spatial location and geomagnetic activity (Kim & Shprits, 2017; Li et al., 2011, 2015; Meredith et al., 2007, 2014, 2012).

Table 1
Satellite Initial Orbits

Satellite	Perigee (km)	Apogee (km)	Inclination (deg)	Period (hr)
DE1	568	23,289	89.9	6.8
Cluster 1	17,200	120,500	90.7	57
TC1	562	78,970	28.2	27
THEMIS-A, THEMIS-D, and THEMIS-E	470	87,330	16.0	31
RBSP-A and RBSP-B	620	30,500	10.0	8.9

Note. DE1 = Dynamics Explorer 1; RBSP = Radiation Belt Storm Probes; THEMIS = Time History of Events and Macroscale Interactions during Substorms.

Accurate modeling thus requires the development of global models of the wave magnetic field intensity for the various relevant wave modes as a function of geomagnetic activity. Improved spatial and temporal coverage may be achieved by combining data from several satellites (Meredith et al., 2012). Here we develop a new model of plasmaspheric hiss by combining data from eight satellites equipped to study plasma waves in the inner magnetosphere. The satellites, associated instrumentation, and data analysis techniques used to develop the model are described in section 2. Methods used to distinguish between plasmaspheric hiss and other wave modes are described in section 3. The global morphology of plasmaspheric hiss as a function of geomagnetic activity is then presented in section 4. Finally, the results are discussed in section and the conclusions are presented in sections 6.

2. Instrumentation and Data Analysis

To build a comprehensive model of plasmaspheric hiss in the inner magnetosphere, we combined plasma wave data from eight satellites. We used approximately 3 years of data from Dynamics Explorer 1 (DE1), 1 year of data from Double Star TC1, 10 years of data from Cluster 1, 17 months of data from each of Time History of Events and Macroscale Interactions during Substorms (THEMIS)-A, THEMIS-D, and THEMIS-E, and 3 years of data from the Van Allen probes, Radiation Belt Storm Probes (RBSP)-A and RBSP-B. The initial orbital parameters of the satellites used in this study are tabulated in Table 1. The instruments, together with the associated frequency ranges and number of frequency channels, are tabulated in Table 2. The observational periods of the missions used to build the wave database are plotted in Figure 1 (top panel). A trace of the 27-day average sunspot number is included in this panel, to show the coverage of the various satellites with respect to the phase of the solar cycle. For reference, traces of the daily averaged *AE* and *Dst* indices, which are measures of substorm and storm activity, respectively, are also included in Figure 1 (middle and bottom panels). In terms of the phase of the solar cycle, the data from DE1 and Double Star TC1 were recorded during the declining phase of solar cycles 21 and 23, respectively, the THEMIS data were collected during the ascending phase of solar cycle 24, the data from the Van Allen probes were collected during the maximum of solar cycle 24, and the Cluster data were recorded over an entire solar cycle. Different types geomagnetic activity are thus well represented in our study, including geomagnetic storms driven by coronal mass ejections that peak during solar maximum (St. Cyr et al., 2000), geomagnetic storms driven by high speed solar wind streams that maximize in the declining phase (Burlaga & Lepping, 1977; Gonzalez et al., 1999), isolated substorms, and the geomagnetically quiet period around the solar minimum in 2009.

Table 2
Instrumentation

Satellite	Instrument	Frequency range	Number of frequency channels
DE1	PWI SFR	105 Hz to 410 kHz	128
Cluster 1	STAFF	8 Hz to 4 kHz	27
TC1	STAFF	8 Hz to 4 kHz	27
THEMIS-A, THEMIS-D, and THEMIS-E	SCM	0.1 Hz to 4 kHz	32
RBSP-A and RBSP-B	EMFISIS WFR	10 Hz to 12 kHz	65

Note. DE1 = Dynamics Explorer 1; RBSP = Radiation Belt Storm Probes; THEMIS = Time History of Events and Macroscale Interactions during Substorms; PWI SFR = Plasma Wave Instrument Step Frequency Receiver; STAFF = Spatiotemporal Analysis of Field Fluctuations; SCM = Search Coil Magnetometer; EMFISIS WFR = Electric and Magnetic Field Instrument and Integrated Science Waveform Receiver; Inc. = Inclination.

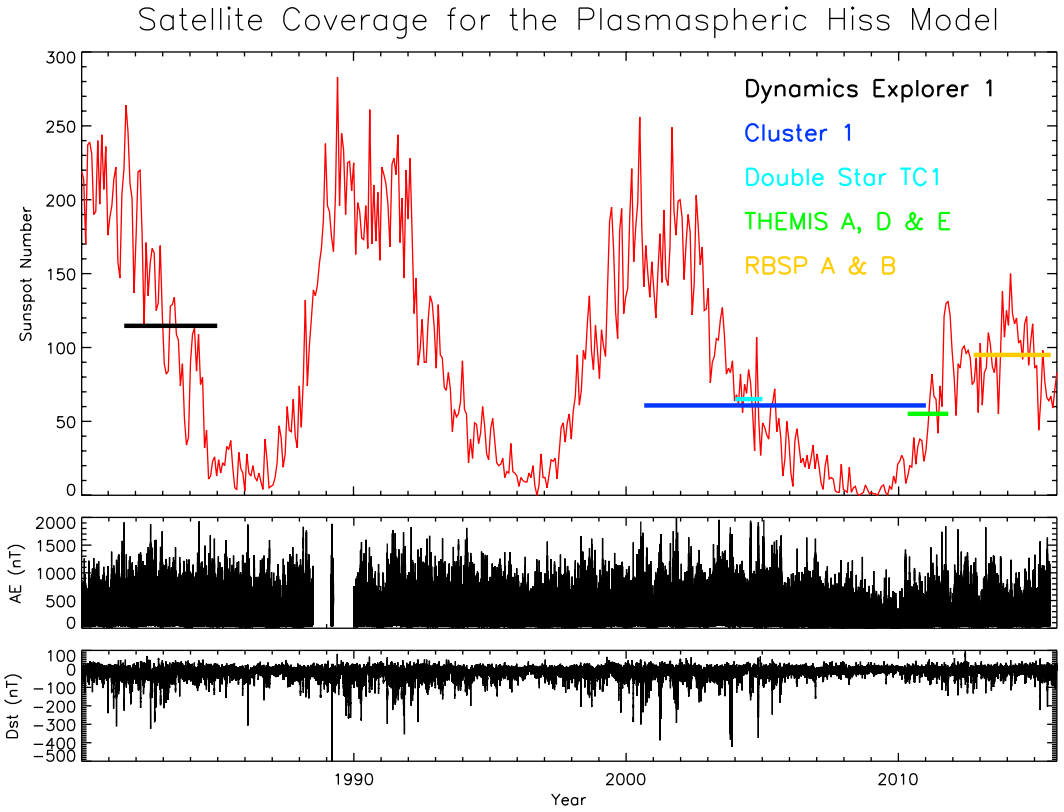

Figure 1. Satellite coverage for the global model of plasmaspheric hiss together with traces of (top) the 27-day average sunspot number, (middle) the daily averaged *AE* index, and (bottom) the daily averaged *Dst* index.

Our previous model of plasmaspheric hiss (Meredith et al., 2004), based on CRRES plasma wave observations, ordered the data using AE^*, the maximum value of the hourly averaged *AE* index in the previous 3 hr, to order the observations of plasmaspheric hiss. At the time plasmaspheric hiss was thought to be generated locally by electrons in the energy range 10–100 keV (e.g., Church & Thorne, 1983). This time delay took into the account the finite drift time of the electrons from their injection region on the nightside to the prenoon sector in the region $2 < L^* < 4$. However, more recent observations show that chorus, in the prenoon sector, is the likely source of the bulk of plasmaspheric hiss (Bortnik et al., 2008, 2009; Chen et al., 2012a, 2012b). During active conditions injected electrons with energies of the order 10–100 keV can rapidly drift to this region on a timescale of less than 1 hr (e.g., Chen et al., 2003). Indeed, chorus is well ordered by the hourly averaged value of *AE* (Meredith et al., 2001, 2012). Since chorus rapidly evolves into plasmaspheric hiss, on a timescale of tens of seconds (e.g., Bortnik et al., 2008), we use the hourly averaged *AE* index as opposed to AE^* to order the data in this study.

Details of the methods used to analyze the wave data from DE1, Double Star TC1, and THEMIS A, D and E are given in Meredith et al. (2012) and those used to analyze the RBSP-A and RBSP-B wave data are given in Li et al. (2015). For each satellite the average magnetic field wave intensity and the corresponding number of samples were binned as a function of fixed frequency band, L^*, MLT magnetic latitude (λ_m) and geomagnetic activity as recorded by the *AE* index. L^*, which is related to the third adiabatic invariant (Roederer, 1970), and MLT were computed using the Olson-Pfitzer quiet time model (Olson & Pfitzer, 1977) and the International Geomagnetic Reference Field (IGRF) field at the middle of the appropriate year. Since L^* is calculated for particles and we are using it for waves we assumed a local pitch angle of 90° in the determination of L^*. The magnetic latitude was calculated using a simple dipole magnetic latitude. The nine fixed frequency bands used to determine the plasmaspheric hiss wave power were 10 to 20, 20 to 50, 50 to 100, 100 to 200, 200 to 500, 500 to 1,000, 1,000 to 2,000, 2,000 to 3,000 and 3,000 to 4,000Hz. The bin ranges are tabulated in Table 3, and the definition of the geomagnetic activity levels used in this study are tabulated in Table 4. We then combined the data from each of the satellites, weighting the data in each bin from each individual satellite by the corresponding number of samples, to create a combined wave database as a function of frequency band, L^*, MLT, λ_m, and geomagnetic activity.

Table 3
Format of the Wave Model

Parameter	Bins
L^*	90 linear steps from $L^* = 1$ to $L^* = 10$
MLT	24 linear steps from 0 to 24 MLT
λ_m	60 linear steps from −90° to 90°
Activity	10 activity levels as monitored by *AE*

Note. MLT = magnetic local time.

3. Identification of the Wave Mode

In the inner magnetosphere, plasmaspheric hiss which is typically observed in the frequency range from several tens of hertz to several kilohertz (Li et al., 2015) can overlap in frequency with magnetosonic waves, which are observed at frequencies between the proton gyrofrequency and the lower hybrid resonance frequency (Russell et al., 1970; Santolík et al., 2004). For the Van Allen probes wave data we excluded magnetosonic waves, which typically have large wave normal angles and hence low ellipticity values, by excluding waves with ellipticity less than 0.7. We do not routinely have information on the ellipticity for the wave data from the other satellites, and so for these satellites, a different technique is required to exclude magnetosonic waves. Gurnett (1976) analyzed equatorial crossings in the region $2.0 < L < 3.5$ and found that the waves were mostly restricted to within 3° of the magnetic equatorial plane. For the other satellites we, therefore, excluded emissions observed within ±3° of the magnetic equator.

Plasmaspheric hiss can also overlap in frequency with whistler mode chorus, which is typically observed in the frequency range from 0.1 to $0.8f_{ce}$ (Koons & Roeder, 1990; Tsurutani & Smith, 1977), where f_{ce} is the electron gyrofrequency. Thus, we cannot distinguish between plasmaspheric hiss and chorus based on frequency alone. However, plasmaspheric hiss tends to be confined to high-density regions associated with the plasmasphere (e.g., Thorne et al., 1973) and plasmaspheric plumes (e.g., Summers et al., 2008), whereas whistler mode chorus waves are largely confined to the low-density region of the plasma trough (Meredith et al., 2001; Tsurutani & Smith, 1977). In previous studies using CRRES plasma wave data a criterion based on the presence or absence of electron cyclotron harmonic (ECH) waves was used to define whether a particular observation was inside or outside the plasmapause, since ECH waves tend to be excluded from the plasmasphere and plasmaspheric plumes (e.g., Meredith et al., 2004; Meredith, Horne, Glauert, et al., 2006). Specifically, we used the criterion that the ECH wave amplitude for frequencies in the range $f_{ce} < f < 2f_{ce}$ must be less than or greater than 0.0005 mVm^{-1} for an observation to be inside or outside the plasmapause respectively. However, this method cannot be used for our global multisatellite model as some of the satellites did not measure ECH waves.

A method to distinguish between plasmaspheric hiss and chorus, which can be universally applied to each satellite data set, is therefore required. Figure 2 shows the global distribution of waves in the 200 to 500 Hz frequency band in the near-equatorial region, $0° < |\lambda_m| < 15°$, as a function of L^* and MLT for the five levels of geomagnetic activity tabulated in Table 4. Each plot is oriented such that noon is at the top and dawn is to the right and extends linearly out to $L^* = 10$. The average intensities are shown in the large panels and the corresponding sampling distributions in the small panels. Two clear populations of waves can be seen. An inner population that peaks on the dayside during active conditions, $400 < AE < 750$ nT, in the region $2 < L^* < 4$, consistent with previous observations of equatorial plasmaspheric hiss (Meredith et al., 2004) and an outer population that peaks on the dawnside, typically beyond $L^* = 5$ during active conditions from 22 to 13 MLT. The location of the emissions of this second population moves to lower L^* values for higher frequencies (Meredith et al., 2013). Furthermore, the intensities of this second population are greatly reduced in the predawn sector at higher latitudes (Meredith et al., 2013). The local time distribution, varying radial extent as a function of fixed frequency, and latitudinal dependence of the second population are all consistent with previous observations of whistler mode chorus waves (Li et al., 2011; Meredith et al., 2001, 2012, 2013). We can use these two different global distributions to separate plasmaspheric hiss and chorus.

Table 4
Definition of the Geomagnetic Activity Levels for the Wave Study

Level	*AE* (nT)
1	$0 < AE < 50$
2	$50 < AE < 100$
3	$100 < AE < 200$
4	$200 < AE < 400$
5	$400 < AE < 750$

To develop a method to distinguish between plasmaspheric hiss and chorus based on their global distributions, we first plotted the wave intensities as a function of L^* in the near-equatorial region for each MLT sector in steps of 1 hr of MLT for the five geomagnetic activity levels. We found that the resulting plasmaspheric hiss and chorus profiles as a function of L^* could each be represented in Gaussian form with the peak in the chorus profile for any given fixed frequency band moving to smaller L^* with increasing geomagnetic activity. By performing radial fits for the different frequency bands

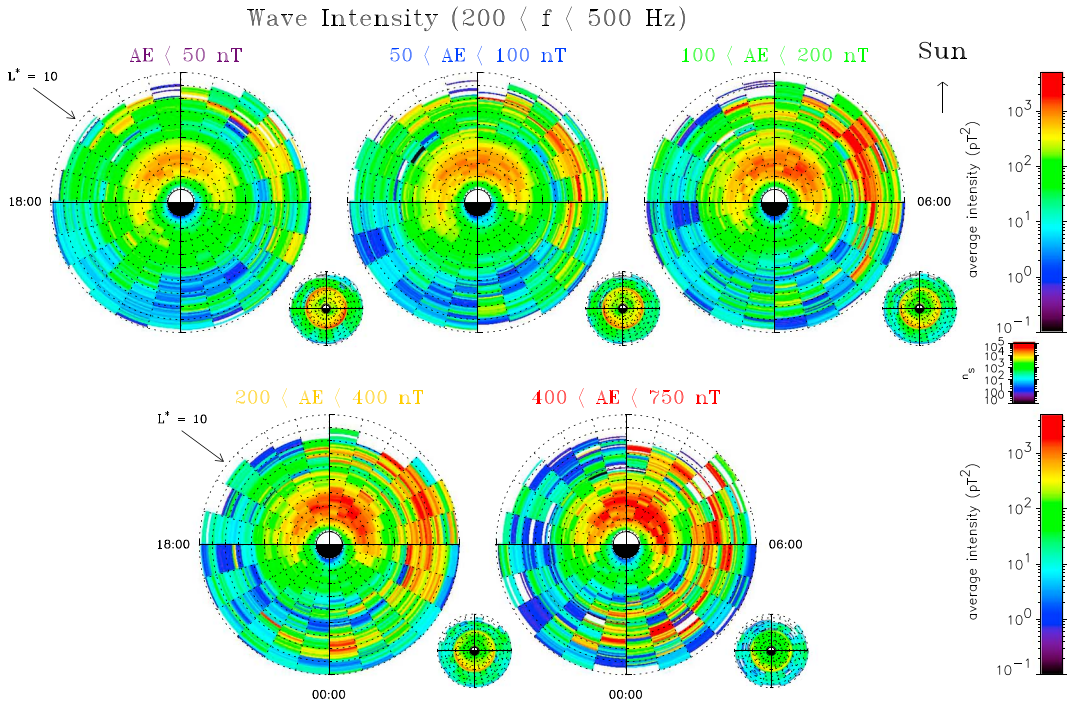

Figure 2. Global maps of the average wave intensity in the 200 to 500 Hz frequency band in the near-equatorial region, $0° < |\lambda_m| < 15°$, as a function of L^* and magnetic local time for five geomagnetic activity levels as monitored by the *AE* index. The maps extend linearly out to $L^* = 10$ with noon at the top and dawn to the right. The average intensities are shown in the large panels and the corresponding sampling distributions in the small panels.

for each hour of MLT, we found that plasmaspheric hiss was best identified in the 200 to 500 Hz frequency band for $AE < 200$ nT and in the 500 to 1,000 Hz band for $AE > 200$ nT. In contrast the chorus was best identified at higher frequencies in the 1,000 to 2,000 Hz frequency band for $AE < 200$ nT and the 2,000 to 3,000 Hz frequency band for $AE > 200$ nT.

To help separate the plasmaspheric hiss and chorus emissions, the L^* profiles of the average intensity of plasmaspheric hiss and chorus were separately fitted with Gaussian profiles for the specified frequency bands. To avoid the inclusion of chorus while fitting to the radial profile of plasmaspheric hiss, the wave intensities above a chosen cutoff value, L^*_{cut}, were set to zero. Similarly, the average intensities below L^*_{cut} were set to zero for fitting to the radial profiles of chorus. By inspection, the value of L^*_{cut} was set to 4.0 for $AE < 400$ nT and to 3.0 for $400 < AE < 750$ nT. The fits were performed using a nonlinear least squares fitting routine for all five levels of geomagnetic activity and for each MLT sector. The boundary between plasmaspheric hiss and chorus was taken as the location where the Gaussian fits intersected. Examples illustrating the process are shown in Figure 3 for $100 < AE < 200$ nT (top panels) and $400 < AE < 750$ nT (bottom panels) for four different MLT sectors. The average intensity of plasmaspheric hiss and whistler mode chorus in the defined frequency bands are shown as a function of L^*, where the dotted lines to the left of L^*_{cut}, depicted by the vertical green lines, represent average intensities of plasmaspheric hiss in the defined frequency band and those to the right represent the average intensities of chorus in the defined frequency band. The solid blue and red lines represent the Gaussian fits to the L^* profiles. The intersection of the two Gaussian fits, shown as a dashed vertical line in each panel, defines the boundary that separates the plasmaspheric hiss wave power from the chorus wave power. The boundary is observed to move to lower L^* with increasing geomagnetic activity and can be thought of as a rough proxy for the plasmapause location.

We created a template to identify plasmaspheric hiss based on the boundary between plasmaspheric hiss and chorus in the region 22–14 MLT for each hour of MLT and each geomagnetic activity level. On the duskside, where chorus waves are typically not present, we used a boundary derived from the CRRES wave measurements using the ECH wave criterion to define the boundary between plasmaspheric hiss and chorus for each of the five geomagnetic activity levels.

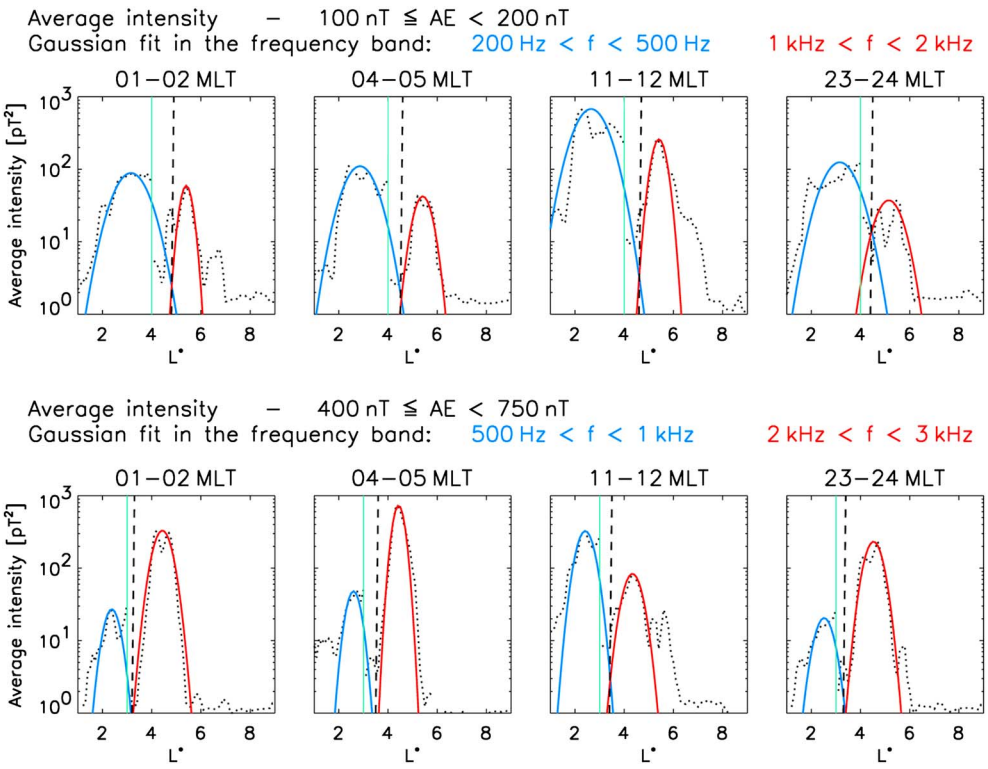

Figure 3. Plot of the average wave intensity (dotted line) as a function of L^* for 100 nT < AE < 200 nT (top row) and 400 nT < AE < 750 nT (bottom row) for four different MLT sectors. The data left of the green line corresponds to the plasmaspheric hiss frequency band (top: 200 Hz < f < 500 Hz, bottom: 500 Hz < f < 1 kHz), while the data right of the green line corresponds to the chorus frequency band (top: 1 kHz < f < 2 kHz, bottom: 2 kHz < f < 3 kHz). The Gaussian fits to the L^* distribution in each band are indicated by the blue and red lines. The intersection of the two Gaussian fits, which defines the boundary that separates the plasmaspheric hiss wave power from the chorus wave power, is shown as a dashed vertical line in each panel.

4. Global Morphology

4.1. MLT Distribution

Figure 4 shows the results of applying the template to the near-equatorial waves in the 200 to 500 Hz frequency band in the same format as Figure 2. Waves on the dawnside at high L^*, attributed to chorus, have been removed, while the waves at lower L^*, attributed to plasmapheric hiss, remain. Consistent with previous studies of plasmaspheric hiss, the largest intensities are typically seen on the dayside, in the region 2.0 < L^* < 4.0, where they are observed to increase with increasing geomagnetic activity.

During quiet conditions, AE < 50 nT, the largest intensities, of the order 500 pT^2 are restricted to the region 2.0 < L^* < 4.0 from 9 to 17 MLT. The largest intensities increase in magnitude and extent as the geomagnetic activity increases with intensities typically exceeding 1,000 pT^2 in the region 1.8 < L^* < 3.7 from 06 to 16 MLT during active conditions, 400 < AE < 750 nT. The average wave intensities are much weaker in the region 20–03 MLT with intensities typically less than 150 pT^2. While the average intensities generally increase with increasing geomagnetic activity, the reverse is true in the premidnight sector, 20–24 MLT, where the average intensities are observed to decrease with increasing geomagnetic activity.

To study the frequency, MLT, and geomagnetic activity dependence of the near-equatorial distribution of plasmaspheric hiss in more detail, line plots of the average wave intensities for the region 1.5 < L^* < 2.5 (bottom) and 2.5 < L^* < 3.5 (top) are shown for each frequency band and each geomagnetic activity level in Figure 5. In the near-equatorial region waves in the 50 to 100 Hz frequency band peak during active conditions with an average intensity of 237 pT^2 in the region 9–13 MLT from 2.5 < L^* < 3.5. Much weaker intensities, typically less than 50 pT^2 are seen on the nightside. At higher frequencies the wave intensities in the 100 to 200 Hz band peak during active conditions with an average intensity of 579 pT^2 in a more extended region 06–15 MLT from 2.5 < L^* < 3.5. The average intensities are largest and most extensive in the 200 to 500 Hz

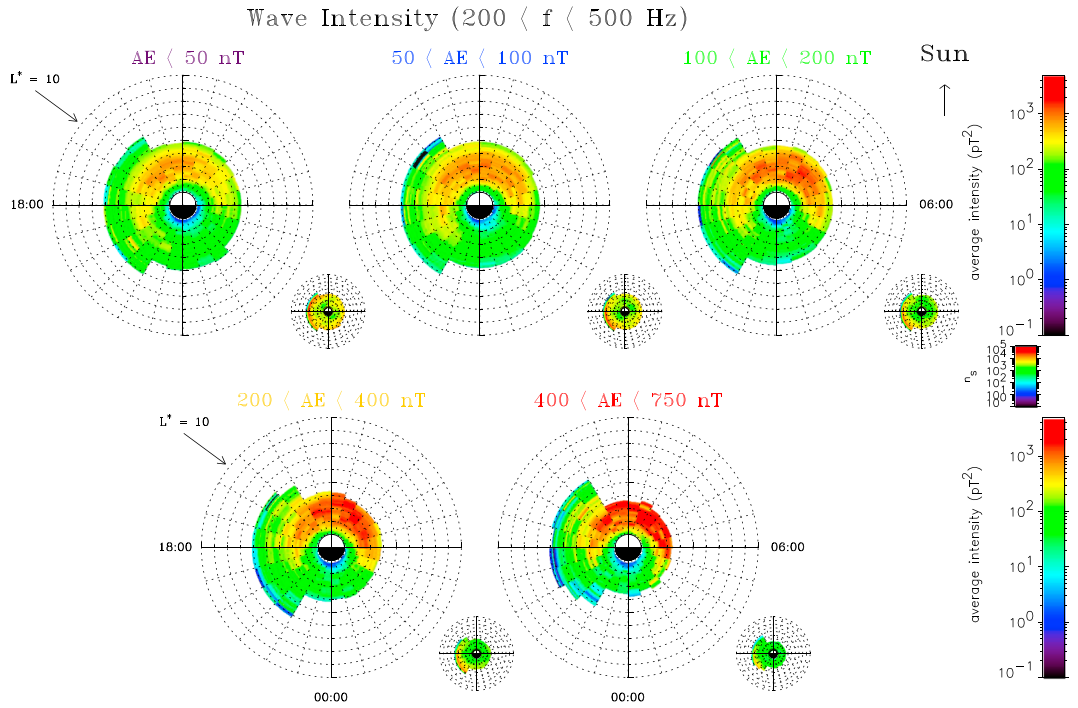

Figure 4. Global maps of the average wave intensity of plasmaspheric hiss in the 200 to 500 Hz frequency band in the near-equatorial region, $0° < |\lambda_m| < 15°$, as a function of L^* and magnetic local time for five geomagnetic activity levels as monitored by the *AE* index. The maps extend linearly out to $L^* = 10$ with noon at the top and dawn to the right. The average intensities are shown in the large panels and the corresponding sampling distributions in the small panels.

frequency band, extending down to $L^* = 1.5$, with an average intensity of 1,128 pT^2 during active conditions in the region 05–17 MLT from $1.5 < L^* < 3.5$. At higher frequencies the average intensities decrease with increasing frequency with, for example, average intensities during active conditions in the region 05–17 MLT from $1.5 < L^* < 3.5$ falling to 357, 99, 12, and 3.1 pT^2 in the 500- to 1,000-, 1,000- to 2,000-, 2,000- to 3,000-, and 3,000 to 4,000 Hz frequency bands, respectively. The tendency for the wave intensity to decrease with increasing geomagnetic activity is evident in the premidnight sector for wave frequency bands up to and including the 500 to 1,000 Hz band.

The global distribution of plasmaspheric hiss as a function of L^* and MLT for different magnetic latitude regions is shown in Figure 6. Here the average wave intensities are shown for, from bottom to top, increasing wave

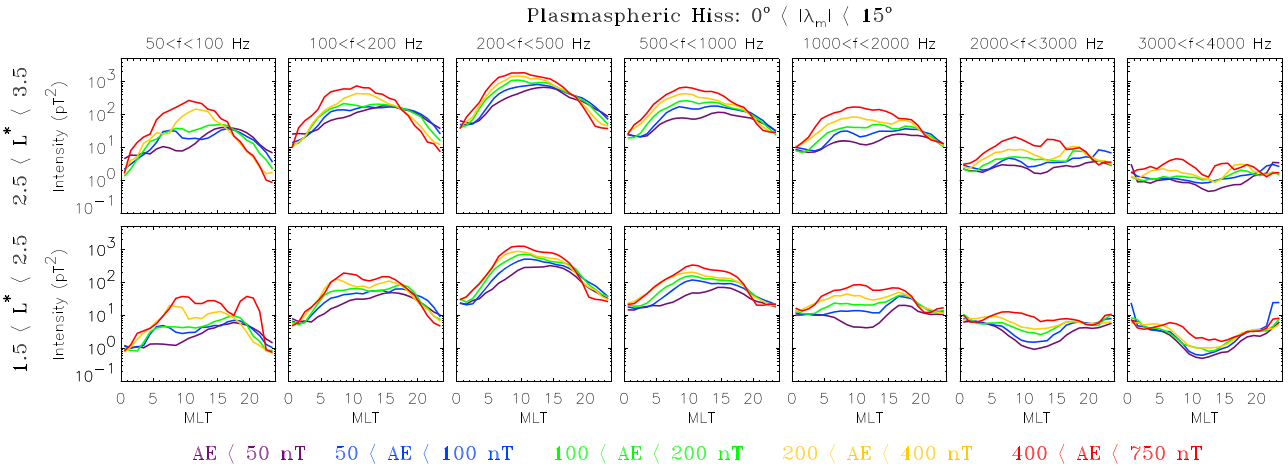

Figure 5. Average wave intensity of plasmaspheric hiss in the near-equatorial region, $0° < |\lambda_m| < 15°$, as a function of MLT for five levels of geomagnetic activity as monitored by the *AE* index for, from left to right, increasing wave frequency for the regions $1.5 < L^* < 2.5$ (bottom row) and $2.5 < L^* < 3.5$ (top row).

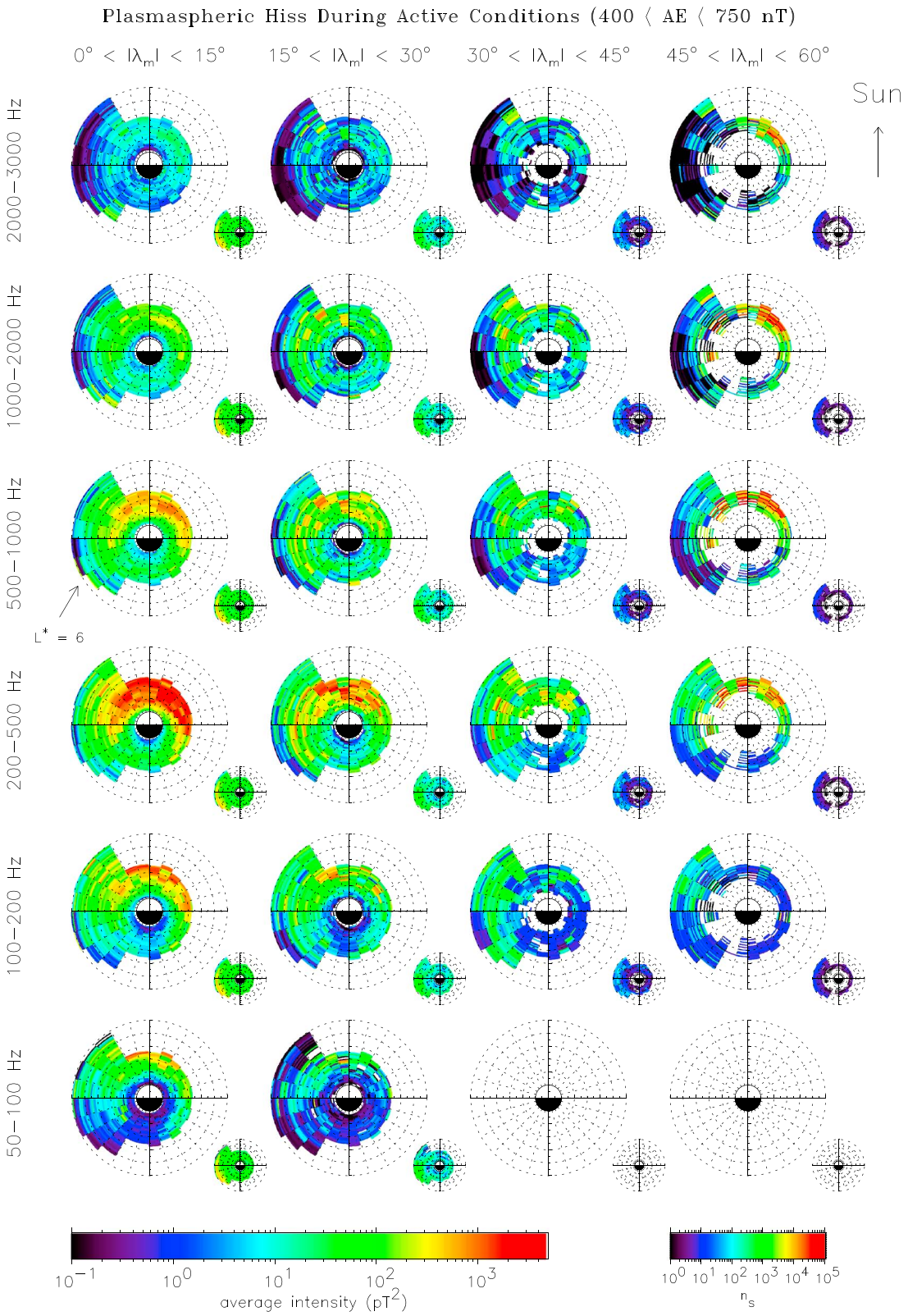

Figure 6. Global maps of the average wave intensity of plasmaspheric hiss as a function of L^* and magnetic local time during active conditions, 400 < *AE* < 750 nT, for, from bottom to top, increasing wave frequency, and for, from left to right, increasing magnetic latitude. The maps extend linearly out to $L^* = 6$ with noon at the top and dawn to the right. The average intensities are shown in the large panels and the corresponding sampling distributions in the small panels.

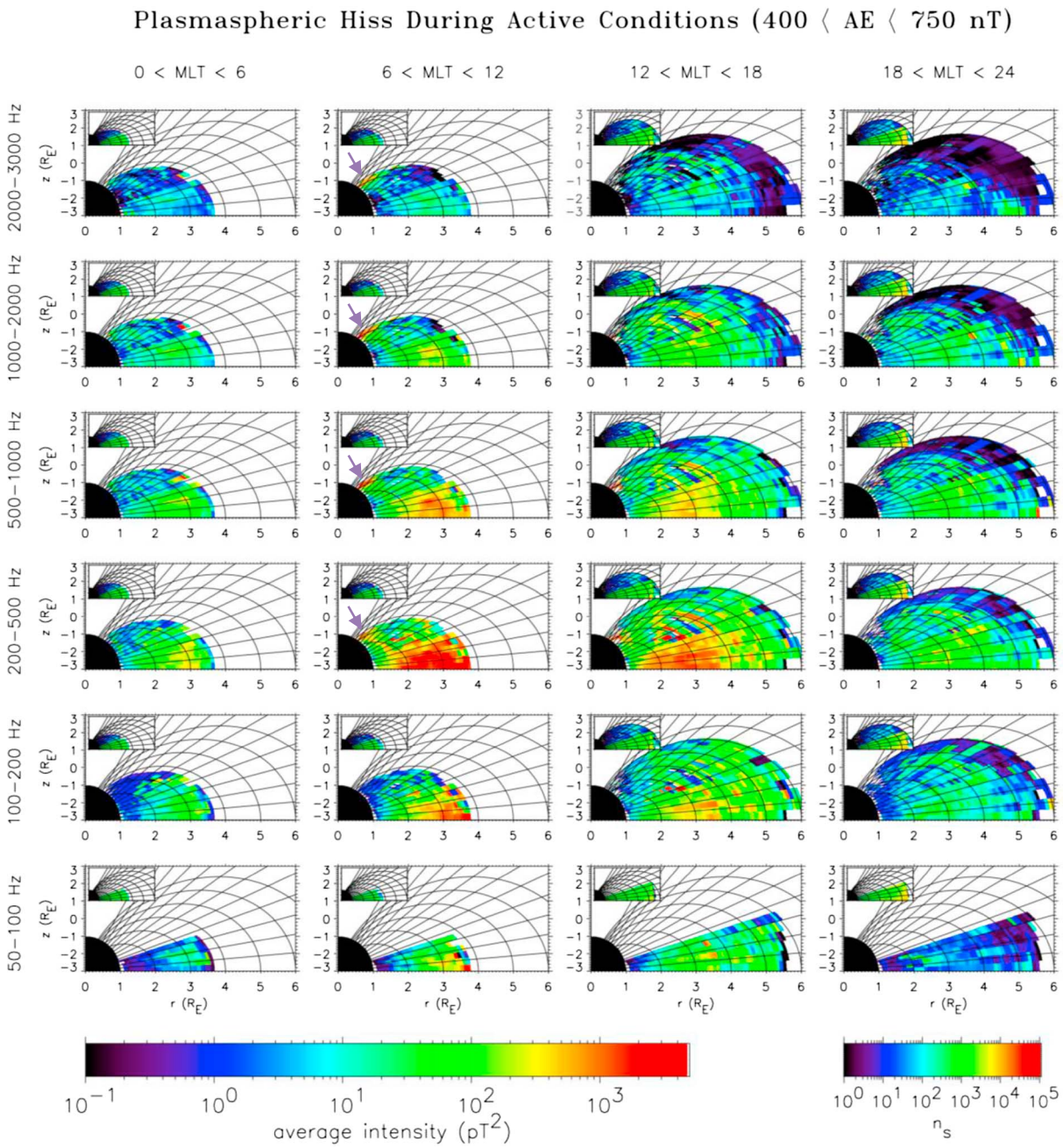

Figure 7. Global maps of the average wave intensity of plasmaspheric hiss in the meridional plane during active conditions, 400 < *AE* < 750 nT, for, from bottom to top, increasing wave frequency and for, from left to right, increasing magnetic local time. To aid visualization of the data, dipole field lines and lines of constant magnetic latitude are included on the plot. The average intensities are shown in the large panels and the corresponding sampling distributions in the small panels. In the prenoon sector the purple arrows point to the location of the high-latitude plasmaspheric hiss.

frequency, and for, from left to right, increasing absolute magnetic latitude. The maps are oriented such that noon is at the top and dawn is to the right and extend linearly out to $L^* = 6$. The average intensities are again shown in the large panels and the corresponding sampling distributions in the small panels. At midlatitudes, $15° < |\lambda_m| < 30°$, the plasmaspheric hiss is again strongest on the dayside in the 200 to 500 Hz frequency band with an average intensity of 413 pT^2 in the region 05–17 MLT from $1.5 < L^* < 3.5$. The average intensities weaken for all frequency bands at higher midlatitudes, $30° < |\lambda_m| < 45°$. However, at the highest latitudes sampled, $45° < |\lambda_m| < 60°$, the average wave intensities intensify again in the prenoon sector for frequencies above 200 Hz.

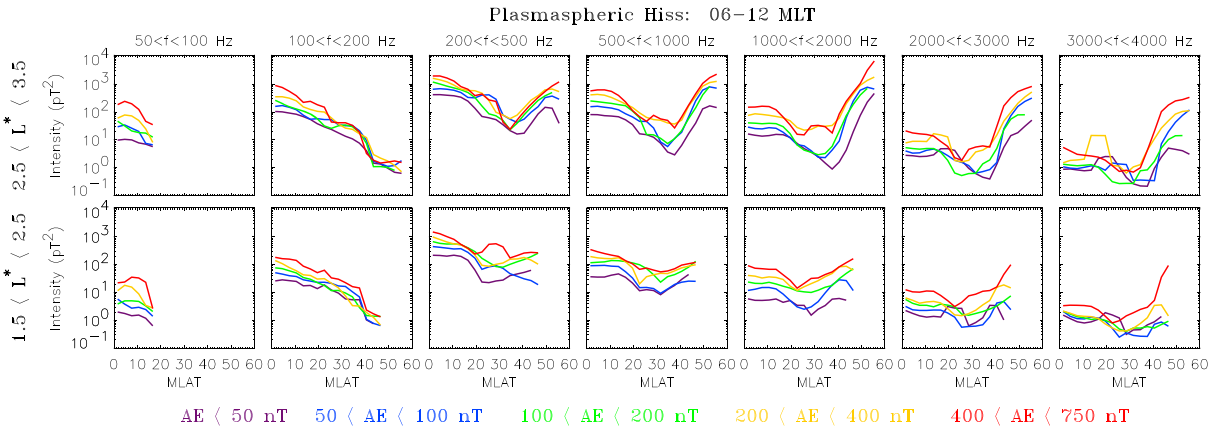

Figure 8. Average wave intensity of plasmaspheric hiss in the prenoon sector as a function of absolute magnetic latitude for five levels of geomagnetic activity as monitored by the *AE* index for, from left to right, increasing wave frequency for the regions $1.5 < L^* < 2.5$ (bottom row) and $2.5 < L^* < 3.5$ (top row).

4.2. Latitudinal Distribution

The latitudinal distribution of plasmaspheric hiss is examined in more detail in Figure 7. Here the average wave intensities during active conditions are plotted in the meridional plane for, from bottom to top, increasing wave frequency and for, from left to right, increasing MLT. The average intensities are shown in the large panels and the corresponding sampling distributions in the small panels. To aid visualization of the data dipole field lines and lines of constant magnetic latitude are included on the plot. The largest intensities are seen in the prenoon sector in the 200 to 500 Hz frequency band, and they tend to be confined to the region $1.7 < L^* < 3.8$ within ±15° of the magnetic equator. A second population of larger intensities, highlighted by the purple arrows (second column from left), are seen at high magnetic latitudes ($45° < |\lambda_m| < 60°$), primarily in the prenoon sector, for frequencies greater than 200 Hz.

To further examine the latitudinal and geomagnetic activity dependence in the prenoon sector, where the waves maximize, the average wave intensities in this sector are plotted as a function of absolute magnetic latitude for the same five levels of geomagnetic activity in Figure 8 for, from left to right, increasing wave frequency for the region $1.5 < L^* < 2.5$ (bottom) and $2.5 < L^* < 3.5$ (top). At low frequencies, waves in the 100 to 200 Hz frequency band peak near the magnetic equator and decrease with increasing magnetic latitude. At higher frequencies the average wave intensities exhibit two peaks, one near the magnetic equator, $0° < |\lambda_m| < 15°$, and one at high latitudes, $45° < |\lambda_m| < 60°$, with a minimum at intermediate latitudes, $30° < |\lambda_m| < 40°$. In the 200 to 500 Hz frequency band in the region $2.5 < L^* < 3.5$ the equatorial and high latitude peak intensities during active conditions are of the same order of magnitude being 1,975 and 1,211 pT^2, respectively. At higher frequencies the equatorial peak during active conditions in the region $2.5 < L^* < 3.5$ decreases with increasing frequency, falling to 575, 149, 21, and 5.4 pT^2 in each consecutive frequency band. In contrast, the high-latitude peak increases with increasing frequency, reaching a peak of 6,794 pT^2 in the 1,000 to 2,000 Hz frequency band before falling to 833 and 337 pT^2 in the two highest frequency bands.

5. Discussion

The average wave intensity of plasmaspheric hiss at frequencies above 200 Hz in the prenoon sector in the region $2.5 < L^* < 3.5$ exhibits maxima near the magnetic equator and at high magnetic latitudes with a minimum in between. The high-latitude power maximum is consistent with a chorus source at higher L^*, since chorus coming in from high L^* tends to focus at higher latitudes and create a power maximum there (e.g., Figure 6 of Bortnik et al., 2011). The waves then spread throughout the plasmasphere with a resulting reduction in intensity (Bortnik et al., 2011). The secondary maximum in the equatorial region cannot be explained by propagation effects alone and is consistent with wave amplification of this embryonic source, ultimately from chorus at higher L^*, by cyclotron resonance inside the plasmasphere (Chen, Li, Bortnik, & Thorne, 2012). The intensities increase with increasing geomagnetic activity at both locations, which is also consistent with a source from chorus at higher L^* values. In the 200 to 500 and 500 to 1,000 Hz frequency bands the equatorial and high-latitude intensities are of a similar order of magnitude. However, at higher frequencies the high-latitude intensities can be up to 2 orders of magnitude higher than the equatorial intensities.

This suggests that the waves that enter the plasmasphere at higher frequencies at high latitude have a greater difficulty in reaching and/or being amplified in the near-equatorial region. Alternatively, there is a possibility that some of the high-latitude emissions at high frequencies could be from penetrating chorus (Bortnik et al., 2007).

In sharp contrast, the average wave intensity of plasmaspheric hiss in the 100 to 200 Hz frequency band in the prenoon sector in the region $2.5 < L^* < 3.5$ show no evidence for a second peak at higher magnetic latitudes. The average wave intensity peaks at around 1,000 pT^2 near the magnetic equator during active conditions and is typically 2 to 3 orders of magnitude higher than that observed at a magnetic latitude of 60°. These results suggest that the source of equatorial plasmaspheric hiss in the 100 to 200 Hz band in the prenoon sector is not chorus propagating into the plasmasphere from higher L shells since waves in this frequency range are not seen at high latitudes. This is consistent with recent findings, which suggest that low-frequency plasmaspheric hiss is a separate population (Malaspina et al., 2017) generated by local amplification by substorm-injected electrons in the outer plasmasphere (Chen et al., 2014; Li et al., 2013; Shi et al., 2017).

The average intensities of plasmaspheric hiss and whistler mode chorus generally increase with increasing geomagnetic activity. However, in the frequency range $50 < f < 1{,}000$ Hz in the in the premidnight sector ($18 < \mathrm{MLT} < 24$) the reverse is true and the average intensities of plasmaspheric hiss are found to decrease with increasing geomagnetic activity. Interestingly, at large L^* ($L^* > \sim 6$) in the postnoon sector ($12 < \mathrm{MLT} < 18$), the chorus intensities also decrease with increasing geomagnetic activity (Meredith et al., 2012). This raises the intriguing possibility that the dominant source of the weak plasmaspheric hiss in the premidnight sector is chorus at larger L^* in the postnoon sector that enters that plasmasphere in the postnoon sector and subsequently propagates eastward in MLT due to strong azimuthal density gradients imposed by the plasmaspheric drainage plume, as first demonstrated by Chen et al. (2009) using a density distribution appropriate for the main phase of a storm. Further evidence in support of this mechanism is to be found in the frequency and MLT dependence. Chorus at high L^* ($L^* > 6$) in the frequency range $0.1-0.3f_{ce}$, which is the dominant frequency range of the chorus source of plasmaspheric hiss (Chen et al., 2012a), typically has an absolute frequency below 1,000 Hz. The trend of decreasing plasmaspheric hiss intensities with increasing geomagnetic activity in the premidnight sector would thus be expected to breakdown above 1,000 Hz, as is observed. Furthermore, the average intensity decreases with increasing MLT in the premidnight sector for all levels of geomagnetic activity, which is also consistent with the eastward migration of rays injected in the prenoon sector.

A previous global model of plasmaspheric hiss based on CRRES observations revealed a second population of waves at midlatitudes, in the latitude range $15° < |\lambda_m| < 30°$ (Meredith et al., 2004). However, no such population is apparent in the new global model based on wave magnetic field measurements alone. The previous model was constructed using a conversion from wave electric to magnetic field intensities based on the cold plasma dispersion relation that assumed parallel propagation at all magnetic latitudes. While this may be true near the magnetic equator, observations and modeling studies shows that the rays become oblique at midlatitudes (e.g., Agapitov et al., 2013; Glauert et al., 2014a; Ni et al., 2013). However, derived intensities for intermediate and large wave normal angles are typically a factor of 1.5 to 5 lower than those assuming parallel propagation respectively (Meredith, Horne, Glauert, et al., 2006). This is confirmed by comparing the new model intensities with those based on CRRES data alone. For example, in the near-equatorial region the average wave intensities on the dayside in the region $2.5 < L^* < 3.5$ for the CRRES model and the new model are similar in magnitude being 1,837 and 1,767 pT^2, respectively. However, at midlatitudes the average intensities on the dayside in the region $2.5 < L^* < 3.5$ for the CRRES model and the new model are 1,951 and 781 pT^2, respectively, suggesting that CRRES observations overestimate the average intensities by a factor of 2.5 in this region. The second population of enhanced intensities at midlatitudes observed by the CRRES satellite was thus most likely due to an overestimation of the wave magnetic field in this region due to obliquely propagating waves. To avoid issues associated with the conversion from wave electric to wave magnetic field, our new global model of plasmaspheric hiss uses direct measurements of the wave magnetic field and excludes the CRRES wave data from the analysis.

More recently, Li et al. (2015) have produced a new global model of plasmaspheric hiss based on Van Allen probe observations. The distribution of plasmaspheric hiss in the near-equatorial region shows a very similar distribution to the current model. However, there is a marked difference, primarily on the dawnside, outside $L^* = 4.0$. If we consider that plasmaspheric hiss is normally observed inside the plasmasphere and chorus outside, then the boundary between plasmaspheric hiss and chorus can be considered to be an approximation

of the plasmapause. Our model then suggests that the plasmasphere typically does not extend beyond $L^* = 4.0$ in this region during moderately active and active conditions. This is consistent with an independent method based on application of the ECH criterion, which shows that the plasmasphere tends to be restricted to the region $L < 4.0$ on the dawnside during active conditions (Meredith et al., 2004) and with an MLT-dependent empirical model of the plasmapause location, based on CRRES density data, of $L = 3.5 \pm 0.7$ in the prenoon sector during active conditions defined as $Kp_{max} = 4$ where Kp_{max} is the maximum value of the Kp index in the previous 12 hr (Moldwin et al., 2002). However, the Li et al. (2015) model show that plasmaspheric hiss intensities are strong out to $L^* = 6.0$ in the prenoon sector during active conditions as defined by $AL^* < -500$ nT. Li et al. (2015) use plasma density measurements determined from the upper hybrid resonance frequency (Kurth et al., 2015) to determine if the observed emission is inside the plasmasphere. Specifically, if the in situ plasma density at the time of any given observation is greater than the larger value of $10x(6.6/L)^4$ and 50 cm^{-3}, the observation is defined to be inside the plasmasphere. In the Li et al. (2015) model, the number of samples at $L > 4$ is extremely small in the dawn sector at 6 MLT. The number of samples tends to increase with increasing local time in the prenoon sector, and this may be due to the presence of plumes. Although plumes typically occur in the afternoon sector, they sometimes occur in the prenoon sector (Darrouzet et al., 2008), which is consistent with the larger number of samples in the afternoon sector than that in the prenoon sector in Figure 2f of Li et al. (2015).

The previous model of plasmaspheric hiss used in the current British Antarctic Survey (BAS) global radiation belt model is based on CRRES observations and does not extend inside $L^* = 2$ (Glauert et al., 2014a). The new model presented here extends down to $L^* = \sim 1.1$ and will enable us to establish the role of plasmaspheric hiss in radiation belt dynamics in the inner radiation belt. While the inner radiation belt is relatively stable, the flux of relativistic electrons may increase significantly during strong geomagnetic storms. For example, during the Halloween storms the inner belt increased significantly, with a factor of 50 increase in the flux of 2–6 MeV electrons at $L = 1.5$ (Baker et al., 2007), producing a "new" inner zone. Further out, at $L = 2.0 \pm 0.2$ the flux increased by as much as 5 orders of magnitude and then decayed quite rapidly back to prestorm values. Knowledge of the wave power of plasmaspheric hiss in the inner zone will enable better modeling of the inner radiation belt following strong geomagnetic storms and permit an assessment of the role of plasmaspheric hiss in electron loss in the inner zone as a function of energy and location.

6. Conclusions

We have developed a new global model of plasmaspheric hiss using data from eight satellites to extend the coverage and improve the statistics of existing models. Our main conclusions are as follows:

1. Geomagnetic activity-dependent templates can be used to separate plasmaspheric hiss from chorus emissions.
2. In the region 22–14 MLT the boundary between plasmaspheric hiss and chorus moves to lower L^* values with increasing geomagnetic activity.
3. The average wave intensity of plasmaspheric hiss is largest on the dayside and increases with increasing geomagnetic activity from midnight through dawn to dusk.
4. Plasmaspheric hiss is most intense and spatially extended in the 200 to 500 Hz frequency band during active conditions, $400 < AE < 750$ nT, with an average intensity of 1,128 pT^2 in the region 05–17 MLT from $1.5 < L^* < 3.5$.
5. In the prenoon sector waves in the 100 to 200 Hz frequency band peak near the magnetic equator and decrease in intensity with increasing magnetic latitude, inconsistent with a source from chorus outside the plasmapause but more consistent with local amplification by substorm-injected electrons.
6. In the prenoon sector waves above 200 Hz exhibit two peaks, one near the magnetic equator, $0° < |\lambda_m| < 15°$, and one at high latitudes, $45° < |\lambda_m| < 60°$, with a minimum at intermediate latitudes, $30° < |\lambda_m| < 40°$, consistent with a source from chorus outside the plasmapause.
7. In the premidnight sector the intensity of plasmaspheric hiss in the frequency range $50 < f < 1{,}000$ Hz decreases with increasing geomagnetic activity. The source of this weak premidnight plasmaspheric hiss is likely to be chorus at larger L^* in the postnoon sector that enters that plasmasphere in the postnoon sector and subsequently propagates eastward in MLT.

The new, multiple-satellite model of plasmaspheric hiss will be used to compute pitch angle and energy diffusion coefficients inside the plasmasphere. The new diffusion coefficients will be incorporated into the BAS

global radiation belt model (Glauert et al., 2014a, 2014b) to improve the modeling and forecasting of the inner and outer radiation belt and the slot region.

Acknowledgments
We acknowledge the CDAWeb (https://cdaweb.sci.gsfc.nasa.gov/index.html/) and the Cluster Active Archive (now the Cluster Science Archive—https://www.cosmos.esa.int/web/csa) for the provision of the wave data of DE1 and Cluster, respectively. We thank LPCEE laboratory (Orléans, France) for their help in the analysis of this wave data. We thank the STAFF-DWP instrument team for provision of the Double Star TC1 data, which is also available at the Cluster Science Archive. We thank NASA contract NAS5-02099 and V. Angelopoulos for use of data from THEMIS Mission. Specifically, we thank O. Le Contel and A. Roux for use of SCM data, which is available from http://themis.ssl.berkeley.edu/data/themis/. We are grateful for the Van Allen Probes data from the EMFISIS instrument obtained from https://emfisis.physics.uiowa.edu/data/index. We acknowledge the NSSDC Omniweb for the provision of the geomagnetic activity indices used in this report. WL would like to acknowledge support from NASA grants NNX17AD15G and NNX17AG07G and the AFOSR grant FA9550-15-1-0158. J. B. would like to acknowledge support from NASA grants NNX14AN85G and NNX16AG21G. The research leading to these results has received funding from the European Union Seventh Framework Programme (FP7/2007-2013) under grant agreements 262468 (SPACECAST) and the Natural Environment Research Council Highlight Topic grant NE/P10738X/1 (Rad-Sat). The global model of plasmapheric hiss described in this paper is archived at the BAS Polar Data Centre and is available on request.

References

Abel, B., & Thorne, R. M. (1998a). Electron scattering loss in Earth's inner magnetosphere, 1. Dominant physical processes. *Journal of Geophysical Research*, *103*(A2), 2385–2396. https://doi.org/10.1029/97JA02919

Abel, B., & Thorne, R. M. (1998b). Electron scattering loss in Earth's inner magnetosphere, 2. Sensitivity to model parameters. *Journal of Geophysical Research*, *103*(A2), 2397–2407. https://doi.org/10.1029/97JA02920

Agapitov, O., Artemyev, A., Krasnoselskikh, V., Khotyaintsev, Y. V., Mourenas, D., Breuillard, H., et al. (2013). Statistics of whistler-mode waves in the outer radiation belt: Cluster STAFF-SA measurements. *Journal of Geophysical Research: Space Physics*, *118*, 3407–3420. https://doi.org/10.1002/jgra.50312

Albert, J. M. (1994). Quasi-linear pitch angle diffusion coefficients: Retaining high harmonics. *Journal of Geophysical Research*, *99*(A12), 23,741–23,745. https://doi.org/10.1029/94JA02345

Albert, J. M., Meredith, N. P., & Horne, R. B. (2009). Three-dimensional diffusion simulation of outer radiation belt electrons during the October 9, 1990, magnetic storm. *Journal of Geophysical Research*, *114*, A09214. https://doi.org/10.1029/2009JA014336

Baker, D. N., Kanekal, S. G., Horne, R. B., Meredith, N. P., & Glauert, S. A. (2007). Low-altitude measurements of 2–6 MeV electron trapping lifetimes at $L \leq L \leq 2.5$. *Geophysical Research Letters*, *34*, L20110. https://doi.org/10.1029/2007GL031007

Bortnik, J., Chen, L., Li, W., Thorne, R. M., & Horne, R. B. (2011). Modeling the evolution of chorus waves into plasmaspheric hiss. *Journal of Geophysical Research*, *116*, A08221. https://doi.org/10.1029/2011JA016499

Bortnik, J., Li, W., Thorne, R. M., Angelopoulos, V., Cully, C., Bonnell, J., et al. (2009). An observation linking the origin of plasmaspheric hiss to discrete chorus emissions. *Science*, *324*(5928), 775–778. https://doi.org/10.1126/science.1171273

Bortnik, J., Thorne, R. M., & Meredith, N. P. (2008). The unexpected origin of plasmaspheric hiss from discrete chorus emissions. *Nature*, *452*, 62–66. https://doi.org/10.1038/nature06741

Bortnik, J., Thorne, R. M., & Meredith, N. P. (2009). Plasmaspheric hiss overview and relation to chorus. *Journal of Atmospheric and Solar Terrestrial Physics*, *71*, 1636–1646. https://doi.org/10.1016/j.jastp.2009.03.023

Bortnik, J., Thorne, R. M., Meredith, N. P., & Santolik, O. (2007). Ray tracing of penetrating chorus and its implications for the radiation belts. *Geophysical Research Letters*, *34*, L15109. https://doi.org/10.1029/2007GL030040

Burlaga, L. F., & Lepping, R. P. (1977). The causes of recurrent geomagnetic storms. *Planetary and Space Science*, *25*, 1151–116. https://doi.org/10.1016/0032-0633(77)90090-3

Carpenter, D. L. (1978). New whistler evidence of a dynamo origin of electric fields in the quiet plasmasphere. *Journal of Geophysical Research*, *83*(A4), 1558–1564. https://doi.org/10.1029/JA083iA04p01558

Chan, K.-W., & Holzer, R. E. (1976). ELF hiss associated with plasma density enhancements in the outer magnetosphere. *Journal of Geophysical Research*, *81*(13), 2267–2274. https://doi.org/10.1029/JA081i013p02267

Chen, L., Bortnik, J., Li, W., Thorne, R. M., & Horne, R. B. (2012a). Modeling the properties of plasmaspheric hiss: 1. Dependence on chorus wave emission. *Journal of Geophysical Research*, *117*, A05201. https://doi.org/10.1029/2011JA017201

Chen, L., Bortnik, J., Li, W., Thorne, R. M., & Horne, R. B. (2012b). Modeling the properties of plasmaspheric hiss: 2. Dependence on the plasma density distribution. *Journal of Geophysical Research*, *117*, A05202. https://doi.org/10.1029/2011JA017202

Chen, L., Bortnik, J., Thorne, R. M., Horne, R. B., & Jordanova, V. K. (2009). Three-dimensional ray tracing of VLF waves in a magnetospheric environment containing a plasmaspheric plume. *Geophysical Research Letters*, *36*, L22101. https://doi.org/10.1029/2009GL040451

Chen, L., Li, W., Bortnik, J., & Thorne, R. M. (2012). Amplification of whistler-mode hiss inside the plasmasphere. *Geophysical Research Letters*, *39*, L08111. https://doi.org/10.1029/2012GL051488

Chen, M. W., Schulz, M., Lu, G., & Lyons, L. R. (2003). Quasi-steady drift paths in a model magnetosphere with AMIE electric field: Implications for ring current formation. *Journal of Geophysical Research*, *108*, 1180. https://doi.org/10.1029/2002JA009584

Chen, L., Thorne, R. M., Bortnik, J., Li, W., Horne, R. B., Reeves, G. D., et al. (2014). Generation of unusually low frequency plasmaspheric hiss. *Geophysical Research Letters*, *41*, 5702–5709. https://doi.org/10.1002/2014GL060628

Church, S., & Thorne, R. M. (1983). On the origin of plasmaspheric hiss: Ray path integrated amplification. *Journal of Geophysical Research*, *88*, 7941–7957.

Cornilleau-Wehrlin, N., Gendrin, R., Lefeuvre, F., Parrot, M., Grard, R., Jones, D., et al. (1978). VLF electromagnetic waves observed onboard GEOS-1. *Space Science Reviews*, *22*, 371–382. https://doi.org/10.1007/BF00210874

Darrouzet, F., De Keyser, J., Décréau, P. M. E., El Lemdani-Mazouz, F., & Vallières, X. (2008). Statistical analysis of plasmaspheric plumes with Cluster/WHISPER observations. *Annales Geophysicae*, *26*, 2403–2417. https://doi.org/10.5194/angeo-26-2403-2008

Dunckel, N., & Helliwell, R. A. (1969). Whistler-mode emissions on the OGO 1 satellite. *Journal of Geophysical Research*, *74*(26), 6731–6385. https://doi.org/10.1029/JA074i026p06371

Fok, M.-C., Horne, R. B., Meredith, N. P., & Glauert, S. A. (2008). Radiation Belt Environment Model: Application to space weather nowcasting. *Journal of Geophysical Research*, *113*, A03S08. https://doi.org/10.1029/2007JA012558

Glauert, S. A., Horne, R. B., & Meredith, N. P. (2014a). Three-dimensional electron radiation belt simulations using the BAS Radiation Belt Model with new diffusion models for chorus, plasmaspheric hiss, and lightning-generated whistlers. *Journal of Geophysical Research: Space Physics*, *119*, 268–289. https://doi.org/10.1002/2013JA019281

Glauert, S. A., Horne, R. B., & Meredith, N. P. (2014b). Simulating the Earth's radiation belts: Internal acceleration and continuous losses to the magnetopause. *Journal of Geophysical Research: Space Physics*, *119*, 7444–7463. https://doi.org/10.1002/2014JA020092

Gonzalez, W. D., Tsurutani, B. T., & Clua de Gonzalez, A. L. (1999). Interplanetary origin of geomagnetic storms. *Space Science Reviews*, *88*, 529–562. https://doi.org/10.1023/A:1005160129098

Gurnett, D. A. (1976). Plasma wave interactions with energetic ions near the magnetic equator. *Journal of Geophysical Research*, *81*, 2765–2770. https://doi.org/10.1029/JA081i016p02765

Kim, K.-C., & Shprits, Y. (2017). Dependence of the amplitude of magnetosonic waves on the solar wind and AE index using Van Allen Probes. *Journal of Geophysical Research: Space Physics*, *122*, 6022–6034. https://doi.org/10.1002/2017JA024094

Koons, H. C., & Roeder, J. L. (1990). A survey of equatorial magnetospheric wave activity between 5 and 8 RE. *Planetary and Space Science*, *38*, 1335–1341. https://doi.org/10.1016/0032-0633(90)90136-E

Kurth, W. S., De Pascuale, S., Faden, J. B., Kletzing, C. A., Hospodarsky, G. B., Thaller, S., & Wygant, J. R. (2015). Electron densities inferred from plasma wave spectra obtained by the Waves instrument on Van Allen Probes. *Journal of Geophysical Research: Space Physics*, *120*, 904–914. https://doi.org/10.1002/2014JA020857

Lam, M. M., Horne, R. B., Meredith, N. P., & Glauert, S. A. (2007). Modeling the effects of radial diffusion and plasmaspheric hiss on outer radiation belt electrons. *Geophysical Research Letters*, *34*, L20112. https://doi.org/10.1029/2007GL031598

Li, W., Bortnik, J., Thorne, R. M., & Angelopoulos, V. (2011). Global distribution of wave amplitudes and wave normal angles of chorus waves using THEMIS wave observations. *Journal of Geophysical Research*, *116*, A12205. https://doi.org/10.1029/2011JA017035

Li, W., Ma, Q., Thorne, R. M., Bortnik, J., Kletzing, C. A., Kurth, W. S., et al. (2015). Statistical properties of plasmaspheric hiss derived from Van Allen Probes data and their effects on radiation belt electron dynamics. *Journal of Geophysical Research: Space Physics*, *120*, 3393–3405. https://doi.org/10.1002/2015JA021048

Li, W., Ma, Q., Thorne, R. M., Bortnik, J., Zhang, X. J., Li, J., et al. (2016). Radiation belt electron acceleration during the 17 March 2015 geomagnetic storm: Observations and simulations. *Journal of Geophysical Research: Space Physics*, *121*, 5520–5536. https://doi.org/10.1002/2016JA022400

Li, W., Thorne, R. M., Bortnik, J., Reeves, G. D., Kletzing, C. A., Kurth, W. S., et al. (2013). An unusual enhancement of low-frequency plasmaspheric hiss in the outer plasmasphere associated with substorm-injected electrons. *Geophysical Research Letters*, *40*, 3798–3803. https://doi.org/10.1002/grl.50787

Lyons, L. R., & Thorne, R. M. (1973). Equilibrium structure of radiation belt electrons. *Journal of Geophysical Research*, *78*(13), 2142–2149. https://doi.org/10.1029/JA078i013p02142

Lyons, L. R., Thorne, R. M., & Kennel, C. F. (1972). Pitch angle diffusion of radiation belt electrons within the plasmasphere. *Journal of Geophysical Research*, *77*(19), 3455–3474. https://doi.org/10.1029/JA077i019p03455

Ma, Q., Li, W., Thorne, R. M., Ni, B., Kletzing, C. A., Kurth, W. S., et al. (2015). Modeling inward diffusion and slow decay of energetic electrons in the Earth's outer radiation belt. *Geophysical Research Letters*, *42*, 987–995. https://doi.org/10.1002/2014GL062977

Malaspina, D. M., Jaynes, A. N., Boulé, C., Bortnik, J., Thaller, S. A., Ergun, R. E., et al. (2016). The distribution of plasmaspheric hiss wave power with respect to plasmapause location. *Geophysical Research Letters*, *43*, 7878–7886. https://doi.org/10.1002/2016GL069982

Malaspina, D. M., Jaynes, A. N., Hospodarsky, G., Bortnik, J., Ergun, R. E., & Wygant, J. (2017). Statistical properties of low-frequency plasmaspheric hiss. *Journal of Geophysical Research: Space Physics*, *122*, 8340–8352. https://doi.org/10.1002/2017JA024328

Meredith, N. P., Horne, R. B., & Anderson, R. R. (2001). Substorm dependence of chorus amplitudes: Implications for the acceleration of electrons to relativistic energies. *Journal of Geophysical Research*, *106*(A7), 13,165–13,178. https://doi.org/10.1029/2000JA900156

Meredith, N. P., Horne, R. B., Bortnik, J., Thorne, R. M., Chen, L., Li, W., & Sicard-Piet, A. (2013). Global statistical evidence for chorus as the embryonic source of plasmaspheric hiss. *Geophysical Research Letters*, *40*, 2891–2896. https://doi.org/10.1002/grl.50593

Meredith, N. P., Horne, R. B., Clilverd, M. A., Horsfall, D., Thorne, R. M., & Anderson, R. R. (2006). Origins of plasmaspheric hiss. *Journal of Geophysical Research*, *111*, A09217. https://doi.org/10.1029/2006JA011707

Meredith, N. P., Horne, R. B., Glauert, S. A., & Anderson, R. R. (2007). Slot region electron loss timescales due to plasmaspheric hiss and lightning generated whistlers. *Journal of Geophysical Research*, *112*, A08214. https://doi.org/10.1029/2006JA012413

Meredith, N. P., Horne, R. B., Glauert, S. A., Baker, D. N., Kanekal, S. G., & Albert, J. M. (2009). Relativistic electron loss timescales in the slot region. *Journal of Geophysical Research*, *114*, A03222. https://doi.org/10.1029/2008JA013889

Meredith, N. P., Horne, R. B., Glauert, S. A., Thorne, R. M., Summers, D., Albert, J. M., & Anderson, R. R. (2006). Energetic outer zone electron loss timescales during low geomagnetic activity. *Journal of Geophysical Research*, *111*, A05212. https://doi.org/10.1029/2005JA011516

Meredith, N. P., Horne, R. B., Kersten, T., Fraser, B. J., & Grew, R. S. (2014). Global morphology and spectral properties of EMIC waves derived from CRRES observations. *Journal of Geophysical Research: Space Physics*, *119*, 5328–5342. https://doi.org/10.1002/2014JA020064

Meredith, N. P., Horne, R. B., Sicard-Piet, A., Boscher, D., Yearby, K. H., Li, W., & Thorne, R. M. (2012). Global model of lower band and upper band chorus from multiple satellite observations. *Journal of Geophysical Research*, *117*, A10225. https://doi.org/10.1029/2012JA017978

Meredith, N. P., Horne, R. B., Thorne, R. M., Summers, D., & Anderson, R. R. (2004). Substorm dependence of plasmaspheric hiss. *Journal of Geophysical Research*, *109*, A06209. https://doi.org/1029/2004JA010387

Moldwin, M. B., Downward, L., Rassoul, H. K., Amin, R., & Anderson, R. R. (2002). A new model of the location of the plasmapause: CRRES results. *Journal of Geophysical Research*, *107*(A11), 1339. https://doi.org/10.1029/2001JA009211

Ni, B., Bortnik, J., Thorne, R. M., Ma, Q., & Chen, L. (2013). Resonant scattering and resultant pitch angle evolution of relativistic electrons by plasmaspheric hiss. *Journal of Geophysical Research: Space Physics*, *118*, 7740–7751. https://doi.org/10.1002/2013JA019260

Olson, W. P., & Pfitzer, K. (1977). Magnetospheric magnetic field modelling annual scientific report (*AFOSR Contract No. F44620-75-c-0033*).

Parrot, M., & Lefeuvre, F. (1986). Statistical study of the propagation characteristics of ELF hiss observed on GEOS 1, inside and outside the plasmasphere. *Annales Geophysicae*, *4*, 363–384.

Roederer, J. G. (1970). *Dynamics of geomagnetically trapped radiation* (166 pp.). New York: Springer-Verlag.

Russell, C. T., Holzer, R. E., & Smith, E. J. (1969). OGO 3 observations of ELF noise in the magnetosphere, 1. Spatial extent and frequency of occurrence. *Journal of Geophysical Research*, *74*(3), 755–777. https://doi.org/10.1029/JA074i003p00755

Russell, C. T., Holzer, R. E., & Smith, E. J. (1970). OGO 3 observations of ELF noise in the magnetosphere. The nature of equatorial noise. *Journal of Geophysical Research*, *75*, 755–768. https://doi.org/10.1029/JA075i004p00755

Santolík, O., Němec, F., Gereová, K., Macúšová, E., de Conchy, Y., & Cornilleau-Wehrlin, N. (2004). Systematic analysis of equatorial noise below the lower hybrid frequency. *Annales Geophysicae*, *22*(7), 2587–2595. https://doi.org/10.5194/angeo-22-2587-2004

Santolík, O., Parrot, M., Storey, L. R. O., Pickett, J. S., & Gurnett, D. A. (2001). Propagation analysis of plasmaspheric hiss using Polar PWI measurements. *Geophysical Research Letters*, *28*, 1127–113. https://doi.org/10.1029/2000GL012239

Shi, R., Li, W., Ma, Q., Reeves, G. D., Kletzing, C. A., Kurth, W. S., et al. (2017). Systematic evaluation of low-frequency hiss and energetic electron injections. *Journal of Geophysical Research: Space Physics*, *122*, 10,263–10,274. https://doi.org/10.1002/2017JA024571

Smith, E. J., Frandsen, A. M. A., Tsurutani, B. T., Thorne, R. M., & Chan, K. W. (1974). Plasmaspheric hiss intensity variations during magnetic storms. *Journal of Geophysical Research*, *79*(16), 2507–2510. https://doi.org/10.1029/JA079i016p02507

St. Cyr, O. C., Plunkett, S. P., Michels, D. J., Paswaters, S. E., Koomen, M. J., Simnett, G. M., et al. (2000). Properties of coronal mass ejections: SOHO LASCO observations from January 1996 to June 1998. *Journal of Geophysical Research*, *105*, 18,169–18,185. https://doi.org/10.1029/1999JA000381

Su, Z., Xiao, F., Zheng, H., & Wang, S. (2011). Radiation belt electron dynamics driven by adiabatic transport, radial diffusion, and wave-particle interactions. *Journal of Geophysical Research*, *116*, A04205. https://doi.org/10.1029/2010JA016228

Subbotin, D., Shprits, Y., & Ni, B. (2010). Three-dimensional VERB radiation belt simulations including mixed diffusion. *Journal of Geophysical Research*, *115*, A03205. https://doi.org/10.1029/2009JA015070

Summers, D., Ni, B., & Meredith, N. P. (2007). Timescales for radiation belt electron acceleration and loss due to resonant wave-particle interactions: 2. Evaluation for VLF chorus, ELF hiss, and electromagnetic ion cyclotron waves. *Journal of Geophysical Research*, *112*, A04207. https://doi.org/10.1029/2006JA011993

Summers, D., Ni, B., Meredith, N. P., Horne, R. B., Thorne, R. M., Moldwin, M. B., & Anderson, R. R. (2008). Electron scattering by whistler-mode ELF hiss in plasmaspheric plumes. *Journal of Geophysical Research*, *113*, A04219. https://doi.org/10.1029/2007JA012678

Summers, D., Omura, Y., Nakamura, S., & Kletzing, C. A. (2014). Fine structure of plasmaspheric hiss. *Journal of Geophysical Research: Space Physics*, *119*, 9134–9149. https://doi.org/10.1002/2014JA020437

Thorne, R. M. (2010). Radiation belt dynamics: The importance of wave-particle interactions. *Geophysical Research Letters*, *37*, L22107. https://doi.org/10.1029/2010GL044990

Thorne, R. M., Church, S. R., Malloy, W. J., & Tsurutani, B. T. (1977). The local time variation of ELF emissions during periods of substorm activity. *Journal of Geophysical Research*, *82*(10), 1585–1590. https://doi.org/10.1029/JA082i010p01585

Thorne, R. M., Li, W., Ni, B., Ma, Q., Bortnik, J., Baker, D. N., et al. (2013). Evolution and slow decay of an unusual narrow ring of relativistic electrons near L∼3.2 following the September 2012 magnetic storm. *Geophysical Research Letters*, *40*, 3507–3511. https://doi.org/10.1002/grl.50627

Thorne, R. M., Smith, E. J., Burton, R. K., & Holzer, R. E. (1973). Plasmaspheric hiss. *Journal of Geophysical Research*, *78*(10), 1581–1596. https://doi.org/10.1029/JA078i010p01581

Thorne, R. M., Smith, E. J., Fiske, K. J., & Church, S. R. (1974). Intensity variation of ELF hiss and chorus driving isolated substorms. *Geophysical Research Letters*, *1*(5), 193–196. https://doi.org/10.1029/GL001i005p00193

Tsurutani, B. T., Falkowski, B. J., Pickett, J. S., Santolik, O., & Lakhina, G. S. (2015). Plasmaspheric hiss properties: Observations from Polar. *Journal of Geophysical Research: Space Physics*, *120*, 414–431. https://doi.org/10.1002/2014JA020518

Tsurutani, B. T., & Smith, E. J. (1977). Two types of magnetospheric ELF chorus and their substorm dependencies. *Journal of Geophysical Research*, *82*, 5112–5128. https://doi.org/10.1029/JA082i032p05112

Tsurutani, B. T., Smith, E. J., & Thorne, R. M. (1975). Electromagnetic hiss and relativistic electron losses in the inner zone. *Journal of Geophysical Research*, *80*(4), 600–607. https://doi.org/10.1029/JA080i004p00600

Tu, W., Cunningham, G. S., Chen, Y., Morley, S. K., Reeves, G. D., Blake, J. B., et al. (2014). Event-specific chorus wave and electron seed population models in DREAM3D using the Van Allen Probes. *Geophysical Research Letters*, *41*, 1359–1366. https://doi.org/10.1002/2013GL058819

Varotsou, A., Boscher, D., Bourdarie, S., Horne, R. B., Glauert, S. A., & Meredith, N. P. (2005). Simulation of the outer radiation belt electrons near geosynchronous orbit including both radial diffusion and resonant interaction with whistler-mode chorus waves. *Geophysical Research Letters*, *32*, L19106. https://doi.org/10.1029/2005GL023282

Varotsou, A., Boscher, D., Bourdarie, S., Horne, R. B., Meredith, N. P., Glauert, S. A., & Friedel, R. H. (2008). Three-dimensional test simulations of the outer radiation belt electron dynamics including electron-chorus resonant interactions. *Journal of Geophysical Research*, *113*, A12212. https://doi.org/10.1029/2007JA01286